

Decoding Visual Experience and Mapping Semantics through Whole-Brain Analysis Using fMRI Foundation Models

Yanchen Wang^{1*} Adam Turnbull^{1*} Tiange Xiang² Yunlong Xu³
Sa Zhou¹ Adnan Masoud⁴ Shekoofeh Azizi⁵ Feng Vankee Lin^{1†}
Ehsan Adeli^{1,2†}

¹Department of Psychiatry and Behavioral Sciences, Stanford University, Stanford, CA, USA

²Department of Computer Science, Stanford University, Stanford, CA, USA

³Department of Neurobiology, University of Chicago, Chicago, IL, USA

⁴UST, Tampa, FL, USA

⁵ Google DeepMind, Toronto, Ontario, Canada

*Co-lead authors †Corresponding authors: {fvlin, eadeli}@stanford.edu

Abstract

Neural decoding, the process of understanding how brain activity corresponds to different stimuli, has been a primary objective in cognitive sciences. Over the past three decades, advancements in functional Magnetic Resonance Imaging (fMRI) and machine learning have greatly improved our ability to map visual stimuli to brain activity, especially in the visual cortex. Concurrently, research has expanded into decoding more complex processes like language and memory across the whole brain, utilizing techniques to handle greater variability and improve signal accuracy. We argue that “seeing” involves more than just mapping visual stimuli onto the visual cortex; it engages the entire brain, as various emotions and cognitive states can emerge from observing different scenes. In this paper, we develop algorithms to enhance our understanding of visual processes by incorporating whole-brain activation maps while individuals are exposed to visual stimuli. We utilize large-scale fMRI encoders and Image generative models (encoders & decoders) pre-trained on large public datasets, which are then fine-tuned through Image-fMRI contrastive learning. Our models hence can decode visual experience across the entire cerebral cortex, surpassing the traditional confines of the visual cortex. Using a public dataset (BOLD5000), we first compare our method with state-of-the-art approaches to decoding visual processing and show improved predictive semantic accuracy by **43%**. A network ablation analysis suggests that beyond the visual cortex, the default mode network contributes most to decoding stimuli, in line with the proposed role of this network in sense-making and semantic processing. Additionally, we implemented zero-shot imagination decoding on an extra validation dataset, achieving a p-value of **0.0206** for mapping the reconstructed images and ground-truth text stimuli, which substantiates the model’s capability to capture semantic meanings across various scenarios. These findings underscore the potential of employing comprehensive models in enhancing the nuanced interpretation of semantic processes.

Keywords: Computer Vision, Cognitive Science, Artificial Intelligence, Generative Models

1 Main

Understanding the relationship between brain activity and the characteristics of external stimuli, commonly known as “neural decoding” [26] or identifying “neural representations,” [28] is fundamental to advancing neuroscience. In the last three decades, the development and continuous improvement of functional magnetic resonance imaging (fMRI) allowed researchers to map spatial patterns of activity at the level of millimeter-cubed “voxels” onto patterns of stimuli to understand where in the brain information about different stimuli characteristics is held. The majority of this research has focused on mapping representations of visual stimuli onto the visual cortex with increasing success [10, 26, 49, 53]. The field of visual decoding has progressed steadily in terms of the accuracy with which stimuli can be predicted based on brain activity. Still, the pace of this progress has sped up with the recent improvements in

machine learning and deep learning methods that can identify more complex relationships between visual activity and visual stimuli [10, 37, 49, 53]. While recent advances in neural decoding have significantly enhanced the ability of models to reconstruct visual stimuli from neural activities in the *visual cortex*, these models predominantly excel at capturing basic, low-level visual features such as edges, textures, and other pixel-wise attributes [4, 26]. Yet, they struggle to decode the semantics of visual input [10], which is crucial for the understanding of the *visual experience*.

Running parallel to this work has been attempts to map the representations of more complex higher-order processes such as language [2], semantics [25], movie-watching [20], or autobiographical memory [3] onto either specific networks known to be involved in these processes, or more recently the whole brain [41]. Since these representations vary significantly across individuals both in terms of their functional units and spatial arrangements, these works collect datasets that sample more participants than those used in visual studies and statistical approaches such as multi-voxel pattern analysis [36] or representational similarity analysis [29] are leveraged to capture between-subject representation and variance. Recent evidence increasingly suggests that whole-brain processing plays a crucial role in many fundamental tasks, including visual perception. For example, one study suggests that there is a retinotopic code in the default mode network that allows a mapping between past experiences and incoming visual information [51]. Another study suggests that visual images are encoded in terms of the actions they afford, represented across the whole brain [56]. Predictive coding [1] and active inference [15] theories propose that all visual processing is subject to a comparison with an internal model of the world provided via top-down connections with higher-order brain regions. This suggests that advances in decoding visual activity will benefit from the inclusion of whole-brain information. However, whole-brain data presents a significantly higher dimensionality, requiring orders of magnitude larger datasets to effectively train machine learning algorithms for neural decoding. This is why methods optimized for visual cortex activity have been successful in decoding visual stimuli—the visual cortex comprises a more constrained set of voxels, allowing smaller and less complex models to perform the task effectively. Expanding decoding efforts to whole-brain data necessitates more sophisticated models and larger datasets to capture the complexity of neural processing across multiple brain regions.

Inspired by these two lines of research and making use of recently developed foundation models [5] that leverage pretraining on large datasets to maximize predictive accuracy in more specialized data, we propose a novel approach to decode visual representations present throughout the whole brain (Fig. 1), referred to as Whole-brain Analysis of Visual Experience (WAVE). It leverages the ability of these foundation models [5] to identify between-subjects patterns from large amounts of generic data (e.g., various tasks of fMRI and natural image separately) to improve the predictions of models applied to smaller, more specialized datasets even for tasks that involve large amounts of between-person variance (e.g., mapping semantic representations). First, we compare our method with state-of-the-art approaches to decoding visual processing and show improved predictive accuracy. We highlight that even after removing the visual cortex we can show high predictive accuracy on a traditional visual dataset, emphasizing the importance of whole-brain processing for even simple visual tasks. Subsequently, we enhance our model’s interpretability through post-hoc analyses. Our findings reveal that higher-order cortical hierarchy provides more predictive power for visual scenes with greater complexity. Furthermore, we demonstrate the model’s ability to capture semantic information across different scenarios. We used a separate fMRI imagination dataset where participants gave verbal descriptions followed by fMRI during scenario visualization. Our model excelled at decoding scenarios semantically similar to images from the original dataset. This highlights its capacity to generalize semantic understanding beyond the original training data. This research represents both methodological and conceptual advances: we believe that using these methods can improve the accuracy of brain-stimuli mapping in a way that can be applied across a greater range of datasets. Ultimately, this could lead to more precise modeling of neural processes, gaining novel insights into human cognitive processes.

2 Results

In this study, we explored human visual experiences through fMRI, leveraging an advanced fMRI foundation model and generative model to reconstruct visual stimuli. Unlike previous studies [10, 49, 52] that predominantly focused on the visual cortex, which is already known for its role in visual processing [23, 24], we extended our method and analysis to encompass the entire brain (Fig. 1c). The generated saliency map highlighted the model’s attention on various brain networks and regions. We employed a range of metrics to evaluate the reconstructed images produced by our model, emphasizing semantic accuracy [10], high-level and low-level correlations [37].

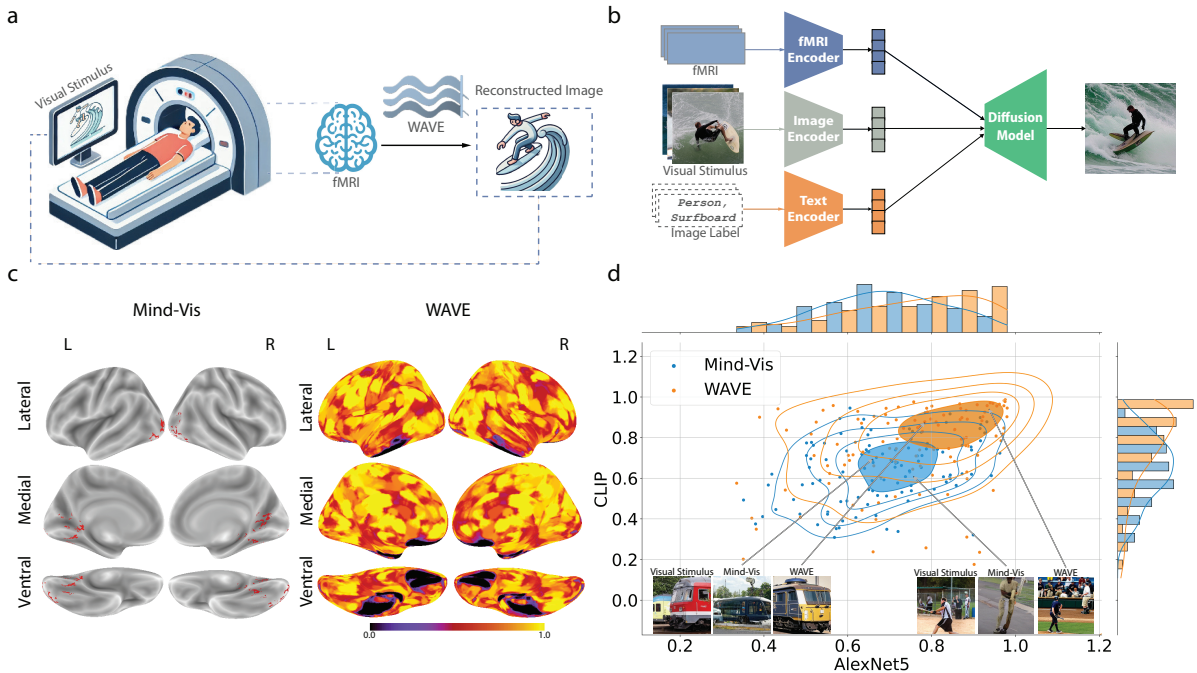


Figure 1: **Model Pipeline and performance comparison with previous work.** **a**, Study Formation: The diagram illustrates our model, WAVE, which reconstructs visual stimuli from fMRI data. **b**, Model Training Framework: After preprocessing the raw fMRI data, WAVE integrates three modalities: fMRI, image, and text to perform contrastive learning. The features are then passed to a diffusion model for final image reconstruction. **c**, Brain Saliency Maps: The saliency maps compare the input fMRI data between Mind-Vis and WAVE (ours). Mind-Vis utilizes only visual cortex data (highlighted in red), whereas WAVE employs whole-brain fMRI data. The saliency map for WAVE is based on the model’s attention, demonstrating a broader and more comprehensive engagement of brain regions. **d**, Quantitative Analysis: This graph compares the performance of the universal model in reconstructing images between Mind-Vis and WAVE. The y-axis represents CLIP accuracy [43] from high-level metrics, and the x-axis represents AlexNet(5) [30] accuracy from low-level metrics [37]. The distributions are displayed on the sides, along with sample images, showcasing the superior performance and robustness of WAVE in capturing both high-level and low-level features.

Going beyond the individual model reconstruction typical of previous work [10, 49, 52], we extended our experiment to include a universal setting, wherein a single model decodes neural activities across different subjects neural activities. We conducted qualitative comparison of our approach with another advanced method Mind-Vis in Fig. 1d. We also conducted extensive ablation studies, demonstrating that whole-brain data offers greater semantic advantages over data solely from the visual cortex.

Finally, we analyzed various clusters of images and presented saliency maps from our model, aiding the explainability of our study, and providing insights through cognitive neuroscience statistical analysis.

2.1 Decoding images from whole-brain fMRIs

We successfully decoded images from whole-brain fMRI data using two distinct methods: building individual models for each subject, as done in visual decoding studies such as [10], and constructing a universal model applicable across four subjects (details in Section 4.1). We evaluated our model’s performance by comparing the reconstructed images against the original visual stimuli, the ground-truth, using a range of metrics that examined the semantic meaning, high-level relationships, and low-level pixel-wise distances (details in Section 4.2).

As shown in Table 1, we benchmarked our model, WAVE, with best in class models MindEye [49] and MindVis [10]. The results of individual subject-based models are detailed in Appendix A.1. In both individual and universal settings, WAVE achieved the best performance in Semantic Top-1 Accuracy and high-level metrics. In low-level metrics, WAVE also outperformed in AlexNet(2) and AlexNet(5).

Table 1: **An evaluation of our model’s capability to reconstruct images from fMRI data.** Employing Semantic metrics as Chen et al. in [10], we adopt a 50-way top-1 accuracy approach (chance=2%) over 1000 trials to gauge the fidelity of reconstructed images against the original stimuli. We used a similar setting to previous study, using Low-Level and High-Level metrics. We used pixel-wise correlation (PixCorr) and structural similarity index metrics (SSIM). Additionally, we assess correlation distance using the EfficientNet-B1 (Eff) [54] and SwAV-ResNet50 (SwAV) [8] models. For other metrics, two-way identification (chance=50%) is used for evaluation, consistent with methodologies described by Ozcelik and VanRullen, Scotti et al.. Two experimental setups were investigated: one involving individualized models for each subject, with an average taken across four subjects’ metric results (detailed results in the appendix), and another employing a universal model for all subjects.

Setting	Model	Low-Level				High-Level				Semantic	
		PixCorr↑	SSIM↑	AlexNet(2)↑	AlexNet(5)↑	Incep↑	CLIP↑	Eff↓	SwAV↓	Top-1	Acc↑
Individual	WAVE (Ours)	0.062	0.199	71.61%	79.70%	68.76%	81.54%	0.892	0.552	25.24%	
	MindEye [49]	0.056	0.217	71.11%	77.31%	66.32	69.98%	0.916	0.592	16.85%	
	Mind-Vis [10]	0.074	0.308	67.42%	72.74%	66.97%	70.07%	0.914	0.556	17.66%	
Universal	WAVE (Ours)	0.050	0.194	69.47%	78.31%	68.41%	78.41%	0.902	0.591	20.75%	
	Mind-Vis [10]	0.036	0.272	60.56%	68.92%	64.25%	64.47%	0.938	0.593	9.19%	

Notably, while SSIM and PixCorr metrics measure pixel-wise correlations, all other metrics from both low-level and high-level categories measure encoded image features from models (e.g. AlexNet, CLIP). (See metrics details in Section 4.2) This suggests that our model excels in semantic and high-level image reconstruction. We also provide rich reconstructed image examples comparing WAVE with MindEye and Mind-Vis in Fig. 2a.

Furthermore, the results from the universal decoding setting, as shown in Table 2 underscore WAVE’s superior performance and the advantage of utilizing whole-brain data compared to Mind-Vis [10]. Due to individual variability, brain fMRI data differ significantly between voxels. The same registered voxel in standard space usually does not have the same function across subjects. However, brain regions tend to maintain similar functions across individuals. Our brain-wide network preprocessed fMRI data showed more advantages in universal settings. Additionally, by leveraging the pre-trained foundation fMRI model, WAVE demonstrated better generalization power, highlighting the robustness and adaptability of our approach. The reconstructed examples in Fig. 2b clearly show our model’s consistency of the generated image across four subjects. WAVE can capture the semantic meaning from brain-wide network activity accurately compare with other methods.

Ablation Study We conducted an ablation study to evaluate the performance of our model using different types of fMRI data. The base model used in this study was MindEye, which differs from Mind-Vis in that it does not utilize a pre-trained voxel encoder. Additionally, MindEye employs a Residual MLP Backbone, making it easier to adjust input dimensionality.

As shown in Table 2, whole-brain network data demonstrated significantly better semantic characteristics compared to data derived from visual cortex voxels. In both individual and universal settings, whole-brain fMRI data achieved state-of-the-art results across all high-level metrics. While PixCorr and SSIM metrics relate more to visual cortex area features, the whole-brain data incorporates complementary information from high-hierarchy functional brain regions involved in visual processing. This comprehensive approach highlights the semantic advantages of using whole-brain data for image reconstruction.

Decoding Visual Stimuli Beyond the Visual Cortex The guiding principle of our research is that brain regions beyond the visual cortex contain valuable information crucial for decoding visual experiences. We posit that these non-visual regions primarily encode the semantic aspects of visual stimuli, thus providing essential information for semantic decoding tasks and image reconstruction. To substantiate this claim, we conducted several experiments outlined below:

- **Semantic decoding without visual network.** We utilized the WAVE model to reconstruct images without data from the visual network, as shown in Figure 2d. These reconstructions retained high quality, with the average semantic accuracy across four subjects reaching **18.98%**. In contrast, whole-brain decoding achieved a higher average accuracy of 25.25%, as presented in Table 1. The high quality reconstruction beyond visual cortex suggests non-visual network also includes significant information for visual experiences decoding. Additionally, the saliency map of the top 20 regions for non-visual regions decoding, is displayed in Figure 2c.

Table 2: **Ablation study results comparing whole-brain and visual cortex data using the MindEye model.** The table illustrates that whole-brain data significantly outperforms visual cortex data in semantic metrics across both individual and universal settings. High-level metrics also show superior performance for whole-brain data, indicating that it captures more comprehensive and high-hierarchy functional information for visual processing. While PixCorr and SSIM metrics, related to visual cortex features, are slightly lower for whole-brain data, the overall advantages in semantic and high-level metrics highlight the robustness and effectiveness of using whole-brain fMRI data for model decoding.

Setting	Data	Low-Level				High-Level				Semantic
		PixCorr \uparrow	SSIM \uparrow	AlexNet(2) \uparrow	AlexNet(5) \uparrow	Incep \uparrow	CLIP \uparrow	Eff \downarrow	SwAV \downarrow	Accuracy \uparrow
Individual	Visual Cortex	0.056	0.217	71.11%	77.31%	66.32%	68.11%	0.916	0.592	16.85%
	Whole Brain	0.084	0.215	71.48%	79.49%	68.64%	76.29%	0.908	0.579	19.60%
Universal	Visual Cortex	0.081	0.214	68.32%	73.82%	63.31%	69.75%	0.929	0.609	14.43%
	Whole Brain	0.091	0.213	68.96%	76.67%	66.60%	76.18%	0.903	0.596	18.72%

- Network mask impact ablation:** To evaluate the contribution of the visual network to decoding, we conducted a network ablation study, systematically masking one of the Yeo 7 networks [63] at a time and using the remaining six for decoding. The results for subject CSI-1, depicted in Figure 2e, show that the removal of the visual network results in a significant accuracy reduction, marked by a red dashed line, compared with whole-brain decoding. In contrast, masking any of the other six networks did not affect semantic accuracy to the same extent as masking the visual network. However, the results also revealed that the default mode and dorsal attention networks play important roles in visual decoding, as their removal also resulted in considerable accuracy reductions. Further reconstructed examples of individual network masking are also provided in Figure 2e. This is in line with expectations, given that the dorsal attention network is adjacent to the visual network and performs higher order visual functions, and the default mode network has a key role in semantic processing and “making sense” of visual input [64].

2.2 Post-hoc analysis of Whole Brain Visual Experience

To showcase our model’s capability in decoding visual experiences, we performed an extensive post-hoc analysis of whole-brain visual experiences using our WAVE model. Employing a self-supervised approach, we clustered original images into five distinct groups and analyzed the corresponding patterns of brain activity. As illustrated in Fig. 3, the brain saliency maps highlight the regions of interest (ROIs) activated by each image cluster. These findings reveal that different clusters are associated with distinct neural activation patterns, but also demonstrate that similar brain networks were important for decoding across different clusters.

2.3 Zero-Shot Human Imagination Decoding

To assess the WAVE model’s capability in decoding semantic meanings from human brain activities, we conducted a zero-shot analysis using an imagination fMRI dataset. This analysis involved reconstructing images from 24 young adults’ imaginations and comparing them with corresponding ground truth textual stimuli. We performed a two-way identification accuracy assessment across 480 paired images and texts, implementing a permutation test to validate the results. Our findings yielded an accuracy of 52%, with a significant p-value of **0.0206**, indicating that our model effectively captures semantic meanings from brain activity associated with text-based imagination.

Additionally, we undertook a scenario-based scale analysis as illustrated in Figure 4. Using a dataset in which participants provided verbal descriptions for scenarios that they later imagined during fMRI, we performed similar decoding of different scenarios using our model. The analysis revealed a correlation between the proximity of scenarios to the training dataset and the accuracy of decoding; specifically, closer cosine distances between scenarios and training data resulted in higher accuracy. For example, “internet” or “movie” scenarios that shared more semantic information with the training images were more easily decoded compared to “barbecue” or “resting” scenarios that were more semantically distinct. This scale analysis suggests that augmenting the training dataset could enhance our model’s ability to decode imagined content by leveraging semantic brain activities, facilitated by the pre-trained whole-brain visual decoding capabilities of the WAVE model. See more Method details in Sec. 4.4.



Figure 2: **Comparison of fMRI data decoding using WAVE and other advanced methods.** a, Reconstructed images using individual model settings for WAVE (Whole Brain), MindEye, and Mind-Vis across the fMRI visual cortex. b, Universal settings across all four subjects in the BOLD5000 dataset. This panel demonstrates the generalization capability of WAVE, MindEye, and Mind-Vis among different subjects. c, The saliency map of the WAVE model using data where the visual cortex has been masked, showing the top 20 regions of interests. d, Decoding from the visual cortex-masked model: examples of reconstructed images using non-visual fMRI regions. In each pair, the left image shows the original visual stimulus, and the right image shows the reconstructed image generated by our visual cortex-masked method (WAVE). e, Impact of network ablation on Decoding Accuracy (subject CSI-1). The left side displays generated images resulting from the masking of each of the seven networks. The right side features a box plot illustrating the decoding accuracy for each network ablation, highlighting the accuracy reduction when specific networks are removed. The red dashed line above represents the whole-brain decoding accuracy for comparison.

3 Discussion

In this paper, we presented a novel approach to decode visual representations present throughout the brain by leveraging a pre-trained foundation model. Compared to the state-of-the-art approaches to decoding visual processing, we found that our model improved on predictive accuracy particularly

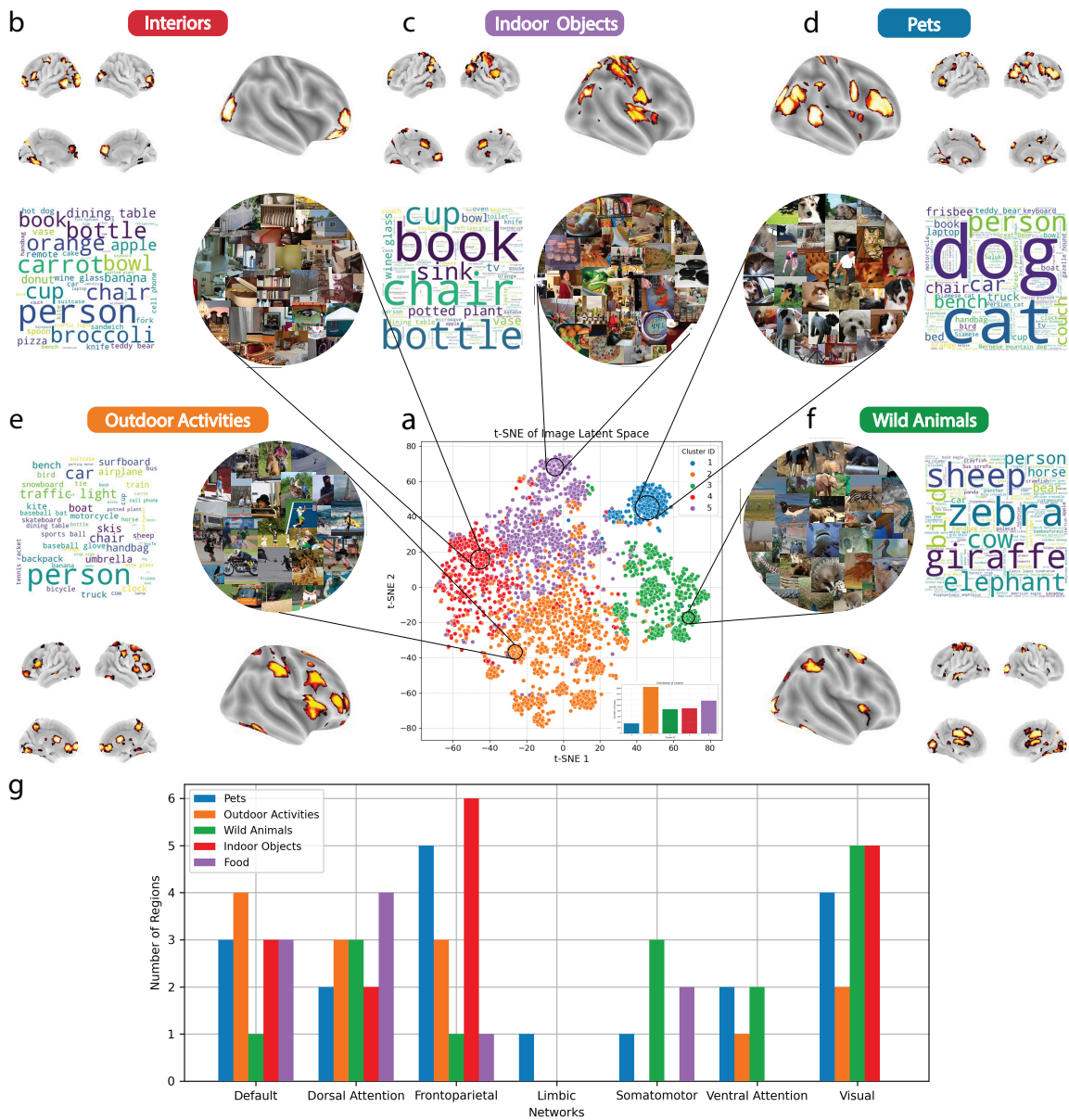


Figure 3: Visualization of Post-Hoc Whole-Brain Visual Clustering Analysis. a, t-SNE visualization of image embeddings, differentiated by five clusters identified via K-Means, each represented in unique colors. b-f, Each subfigure presents word clouds generated from image labels, with word sizes proportional to their frequency of occurrence within the cluster. The subfigure titles, generated by entering the words into ChatGPT-4, summarize the thematic essence of each cluster. Accompanying each word cloud are selected image samples and a whole-brain saliency map highlighting the top 20 regions of interest relevant to the cluster. g, Quantitative analysis showing the distribution of regions across the Yeo 7 networks for each of the five clusters, providing insights into the network-based localization of visual processing associated with different categories.

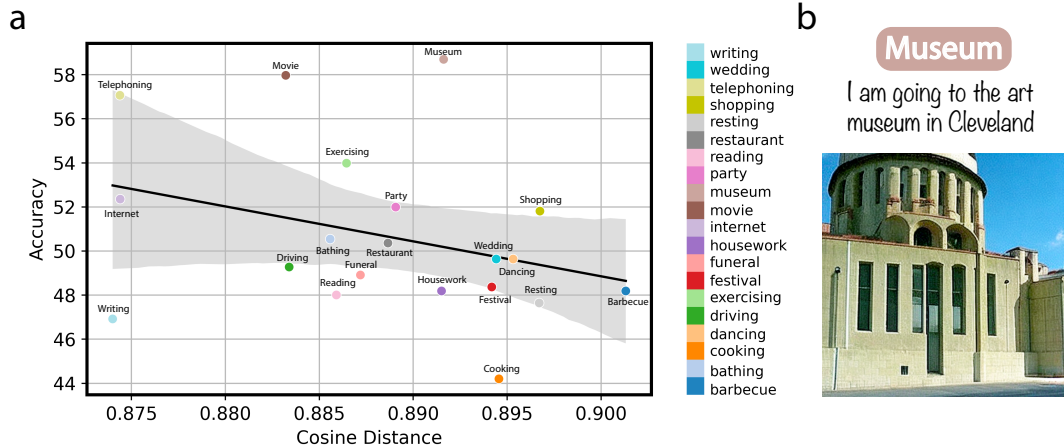


Figure 4: **WAVE Zero-Shot brain imagination decoding results.** a, Scenario-based scale analysis utilizing two-way-identification accuracy. Using a separate dataset ($N=24$ younger adults imagining different scenarios during fMRI), this analysis measures the cosine distance of each scenario’s features to those in the training dataset (BOLD5000). The scatter plot shows the correlation of these cosine distances with decoding accuracy: scenarios that are more similar to the training dataset had more accurate predictions. b, Example of WAVE model zero-shot reconstructed images from imagination recording fMRI sessions. The text stimuli describing the museum scenario are presented above the example image, illustrating the model’s capability to generate visual reconstructions based on described scenarios.

when assessing the higher-level visual and semantic similarity between reconstructed and visual images. Saliency maps visualized regions most important to these predictions and identified predominantly regions in higher-order brain networks such as the frontoparietal and default mode networks, suggesting that higher-order processing was critical to this decoding. In line with this, masking the visual network still produced high levels of accuracy on the same visual decoding task, although it did lead to reductions in accuracy as would be expected. Ablating each network in turn showed that after the visual network, the dorsal attention and default mode networks contributed the most to predictions. This is in line with previous research: the dorsal attention network is adjacent to the visual network and performs higher level visual functions. The default mode network has a key role in semantic processing and “making sense” [64] of visual input, as shown by the presence of a retinotopic code in this network [51]. Post-hoc analyses comparing our model to others suggest that our model was better able to model the semantic information in images due to improved identification of key semantic features, sometimes with an associated loss of accuracy in lower-level visual similarity such as pixel correlation. A scaling analysis in a separate dataset that involved participants making semantic verbal descriptions of scenarios that they imagined during fMRI showed that decoding was improved for scenarios that were more semantically similar to images in the training dataset (e.g., “internet” or “movie” scenarios vs. worse performance for “barbecue” or “resting” scenarios). Overall, these findings highlight that foundation models of fMRI data allow for improved decoding of complex higher-level visual and semantic features in images even when applied to relatively small, specialized datasets that have predominantly traditionally been used to understand lower-level visual processing. We also show that essential information for visual decoding is present in non-visual, higher-order brain networks, particularly the dorsal attention and default mode networks, further emphasizing the role of non-visual regions in visual processing. Our scaling analysis further suggests the importance of semantic information in the performance of this model.

In addition to our primary finding of improved performance over other state-of-the-art approaches, there are several important implications of our work for neuroscience. The ability to improve performance on visual processing using a foundation model trained and applied to the whole brain adds to recent literature highlighting the importance of non-visual regions to visual processing. For example, a recent study identified a retinotopic code in the default mode network that is hypothesized to provide a mapping between past experiences and incoming visual information [51]. This is in line with ideas from predictive coding [1] and active inference [15] theories of the brain that propose incoming visual information is continuously compared to an internal model of the world provided via top-down connections between visual and higher-order brain regions. The default mode network has been proposed to be critical in this

“sense-making” [64], in line with our finding that it contributed more than other non-visual networks to improved predictions. Related work suggests that visual images may be encoded in non-visual regions in terms of the actions they afford [56], in line with theories that consider the fundamental role of the brain to induce actions and predict their consequences as a means of increasing the survival of the individual [7]. Conceptually, our work builds on this by highlighting that higher-order brain networks, particularly the default mode network, contribute critical information to visual decoding and allow for improved separation of visually similar images into distinct clusters based on higher-order visual and semantic information: for example, the separation of wild dogs from domestic dogs.

Our post-hoc explainability analysis also provides some information about exactly which brain regions are contributing to decoding different categories of images. While it is difficult to interpret exactly what certain brain activity patterns mean for the information they represent without engaging in overly speculative reverse inference [40], these data do add important interpretability to our findings in several ways. Breaking down these activation patterns by large-scale brain network, regions in the default mode network were important for all five clusters, in line with the role of this network in semantic processing [6] and matching the results of our network-ablation analysis. The frontoparietal and dorsal attention networks were also important for predictions in all five clusters: these networks are involved in domain-general task-related processing and higher-order visual processing [33, 60] and this analysis suggests they contain information for decoding visual information in various domains. Some clusters did show unique ROIs: limbic regions were only involved in predictions of pets, potentially reflecting the particularly emotional nature of information processing of these images. Sensorimotor regions were most important for decoding the cluster representing wild animals, as shown in Fig. 3g, suggesting a possible additional engagement of areas involved in spatial awareness and movement perception [19] when processing these images. This analysis further emphasizes the importance of whole-brain non-visual regions for visual processing and further suggests that certain images may engage different distributed neural processes depending on their contents.

The final important implication of this work is methodological. We believe that our approach allows for significant further advances in understanding the role of non-visual regions in visual processing by facilitating the mapping of these higher-order processes using foundation models. Moreover, we believe that these models hold significant potential in advancing our understanding of brain-behavior relationships particularly for more complex traits that vary more across people. These models allow us to take advantage of the large amounts of non-specific fMRI data that now exist and may help us improve our predictions of these more complex brain-behavior relationships, beyond functional decoding and into more trait-level brain-behavior analyses. This has huge implications for the field, as these tasks have previously required the collection of either highly specific data or more general data in thousands of individuals [34]. This has led to significant consternation in the field regarding the practicality of using MRI to understand behavior and led some researchers to suggest that data for understanding brain-behavior relationships for complex traits should only be done by consortia [18]. Using similar principles to those proposed by other researchers [22], we believe that foundation models may boost the predictive power of models that aim to predict more variable brain-behavior relationships, reducing the sample size required for individual labs and providing a new “middle path” to robust brain-behavior predictions.

4 Methods

4.1 Dataset

BOLD5000 For our study, we utilized the BOLD5000 dataset, a publicly available fMRI image collection [9]. This dataset comprises fMRI recordings captured as subjects viewed a series of images. The BOLD5000 dataset contains 4,916 unique images, of which 2,000 are sourced from the COCO dataset [32], and 1,916 images are from ImageNet [12]. In each trial, subjects were exposed to each image as a visual stimulus. Among these, 4,803 images were presented once per trial, while 113 images were shown multiple times, either three or four times across several trials, resulting in a total of 5,254 stimulus trials. The dataset documents responses from four subjects, three of whom completed all 5,254 recording trials. In our analysis, we focus on the data from all four subjects who completed the full or partial set of trials.

We adopt the standardized train/test set split employed in existing BOLD5000 image reconstruction studies, as outlined in Chen et al. [10]. For the training set of each subject, we utilized trials with non-repeated image stimuli, encompassing a total of 4,803 samples. For the test set, we consolidated repeated image stimulus trials, resulting in 113 test samples. Furthermore, BOLD5000 provides labels for each image, which we incorporated as the text modality in our analysis.

fMRI Imagination Dataset Additionally, we employed a validation dataset from fMRI imagination recordings as per [3]. This dataset includes 20 different scenarios such as resting, dancing, and museum visits. Subjects provided varied text descriptions for these scenarios. The fMRI data were recorded as subjects imagined themselves in the scenarios prompted by the text descriptions they had written. Each scenario was repeated five times during the fMRI sessions. In our zero-shot analysis, we averaged the fMRI signals from the repeated scenarios to create a single representative signal for each scenario. We engaged 24 young subjects for this study, resulting in a total of $24 \times 20 = 480$ imagination fMRI clips accompanied by text stimuli.

Upstream Datasets In this paper, we utilize a foundational fMRI model incorporating several large-scale fMRI datasets for pre-training [55]. These include the Human Connectome Project [57] and multiple datasets available on OpenNeuro [35], comprising a total of 11,980 fMRI runs from 1,726 individuals across 34 datasets. Additionally, we employed a pre-trained image classifier to evaluate semantic accuracy metrics. This classifier was originally trained on ImageNet1K [47], a dataset that includes approximately 1.2 million images distributed over 1,000 categories, each representing a distinct object or concept.

Preprocessing Functional Magnetic Resonance Imaging (fMRI) data are captured in a four-dimensional space, encompassing three spatial dimensions and one temporal dimension. The Blood-Oxygen-Level-Dependent (BOLD) signals are organized in a sequence denoted as $S = \{V_t | t \geq 0\}$, where t represents the Repetition Time (TR). At each time point t , the volume V_t is represented in a three-dimensional space as $V_t \in \mathbb{R}^{x \times y \times z}$.

We processed all fMRI data using fMRIPrep, following the methodology outlined in Esteban et al. [14], with adaptations to include surface preprocessing. Our preprocessing regimen aligns with the protocols described by Thomas et al. [55] employing the default settings of fMRIPrep with the exception of surface preprocessing. Subsequently, we performed a series of minimal additional processing steps on the derivatives from fMRIPrep. These steps included spatial smoothing of the fMRI sequences, detrending, high-pass filtering, and the removal of confounding factors.

After the preprocessing steps, we parcellated each preprocessed fMRI run using the DiFuMo atlas [11], normalizing the individual network time courses to have a mean of zero and unit variance. We opted for the DiFuMo atlas with 1024 dimensions, effectively transforming each volume $V_t \in \mathbb{R}^{x \times y \times z}$ into a vectorized form $X_t \in \mathbb{R}^{1024}$ as shown in Fig. 5.

In the subsequent step of segmenting BOLD clips, we took into account the hemodynamic effects on BOLD signals [39]. To accommodate the delay introduced by these hemodynamic effects, we adjusted our segmentation to account for a one TR delay. In our dataset configuration, each segmented BOLD clip is characterized by five TRs, resulting in the final fMRI input for our model being $X \in \mathbb{R}^{5 \times 1024}$, where X represents our input data.

4.2 WAVE Model

Our model employs state-of-the-art deep learning [17, 31] and foundation model [5] techniques, structured into two main phases: contrastive learning [43] and diffusion model training [45]. Unlike approaches that merge semi-supervised training methods, our strategy benefits from progressive learning [48]. We initiate with contrastive learning to refine initial insights, followed by the diffusion model phase for enhanced training. Decoding fMRI data poses significant challenges due to its complexity. To address this, we incorporate a pre-trained large fMRI foundation model [55]. In the contrastive learning stage, we integrate image labels as an additional modality, recognizing that label data alone may not provide comprehensive information. To bridge this gap, we employ prompt learning to enrich the text encoder with supplementary image and fMRI details. For the diffusion model training, we introduce a novel approach by employing a diffusion prior [44, 49] to transform fMRI latent representations into image latent representations. This process is completed with a Pre-trained Versatile Diffusion Image Variation Decoder [61], which translates these image latent representations back into visual images. This methodology not only leverages advanced machine learning techniques but also introduces an innovative integration of fMRI data into the image generation process, enhancing the model’s ability to interpret and visualize complex neuroimaging datasets.

fMRI Foundation Model In our research, we adopted a pre-trained Foundation model [55] to serve as the fMRI encoder. This model, structured based on the GPT-2 framework [42], processes the pre-processed fMRI data into fMRI latent representations. As specified in Section 4.1, the input data X ,

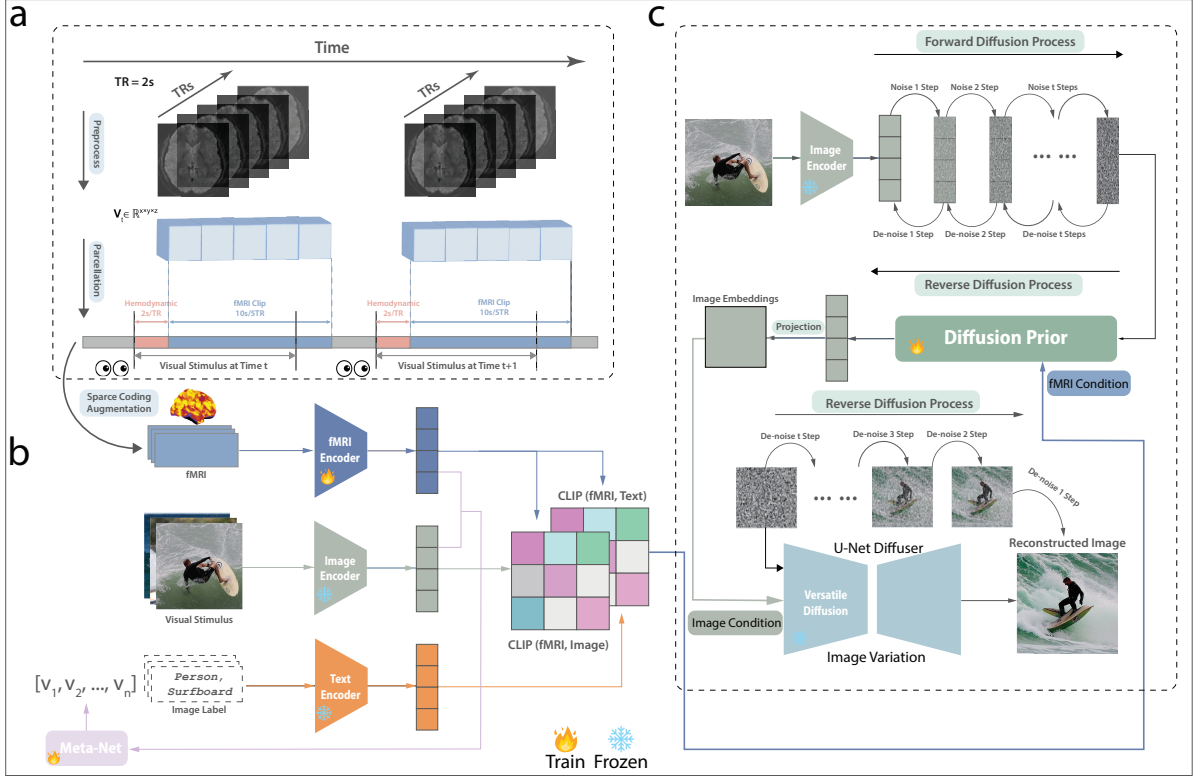


Figure 5: The depicted architecture illustrates the fMRI data processing and a two-part training approach for the model. a, fMRI preprocessing involving network parcellations and BOLD signal segmentation. b, Focus on contrastive learning where knowledge is distilled across three modalities: fMRI, text, and images. c, Training of the diffusion model, which involves fine-tuning a specialized prior to converting fMRI latent representations into image latent variables. Icons of fire and snowflake denote modules that are active (train) and inactive (frozen) during the training phase, respectively.

is conformed to the preprocessed structure $X \in \mathbb{R}^{t \times 1024}$, where 1024 denotes the parcellated brain networks. The fMRI Foundation model employs self-supervised learning (SSL) on extensive fMRI datasets, including the Human Connectome Project [57] and datasets available through OpenNeuro [35]. It assimilates both the sequential temporal fMRI information and TR embeddings, which function similarly to position embeddings [58] to indicate the temporal intervals between fMRI sequences. The self-supervised learning task is to predict the subsequent timepoint sequence given an input sequence X_t ; thus, the model predicts X_{t+1} .

In this study, we processed an fMRI run, retaining the spatial and temporal features to form the input X , where $X \in \mathbb{R}^{5 \times 1024}$. Each fMRI segment has 5 TRs. The attention is on the embedded fMRI sequence. Based on the SSL paradigm, we took the predicted masked token, which is the output $O_t \in \mathbb{R}^{768}$ where $t = 6$. The output O_6 was taken as our encoded fMRI latent features.

Contrastive Learning In this study, we employ multi-modal contrastive learning, capitalizing on the integration of diverse data forms to enrich the feature representation of fMRI scans in a latent space. Our approach is distinct in that it encompasses not only visual data but also textual information through the inclusion of image labels. This incorporation aims to augment the semantic understanding within our model. To facilitate this, we utilize a pre-trained Vision Transformer (ViT) [13] based CLIP model [43], maintaining the integrity of its parameters by freezing them throughout the training phase.

Our implementation introduces CLIP loss within the contrastive learning framework, addressing three different modalities: fMRI-image and fMRI-text. Let the normalized projections of modality as z and a temperature parameter as \mathcal{T} , the CLIP Loss \mathcal{L}_{CLIP} of two modalities z_1, z_2 in batch B is shown in Eq. 1. The computation of contrastive Loss \mathcal{L}_C (Eq. (2)) involves aggregating the losses from fMRI to image and fMRI to text comparisons, followed by averaging the sum. The training regimen proceeded over 50,000 steps utilizing an Adam optimizer, selecting the model state at the final step for subsequent training with a diffusion model.

$$\mathcal{L}_{\text{CLIP}}(z_1, z_2) = -\frac{1}{2|B|} \sum_{i=1}^{|B|} \left[\log \frac{\exp(z_{1_i} \cdot z_{2_i} / \tau)}{\sum_{j=1}^{|B|} \exp(z_{1_i} \cdot z_{2_j} / \tau)} + \log \frac{\exp(z_{2_i} \cdot z_{1_i} / \tau)}{\sum_{j=1}^{|B|} \exp(z_{2_i} \cdot z_{1_j} / \tau)} \right], \quad (1)$$

$$\mathcal{L}_{\mathcal{C}} = (\mathcal{L}_{\text{CLIP}}(z_{\text{fMRI}}, z_{\text{image}}) + \mathcal{L}_{\text{CLIP}}(z_{\text{fMRI}}, z_{\text{text}})) / 2. \quad (2)$$

Furthermore, we assess the efficacy of our training process through contrastive learning accuracy metrics. Detailed explanations of these methodologies and the results are provided in the Appendix.

Prompt Learning To enhance our contrastive learning framework, we were inspired by prompt learning [27, 62, 65] in the AI field, which is particularly effective when text labels serve as one modality in contrastive learning. Text labels, while compact, inherently contain less information than images. Prompt learning, a technique tailored for text encoders, enriches this modality by generating context that extracts more nuanced information from the text. Considering the fMRI, image, and text share the same information. We introduced a lightweight architecture called Meta-Net designed to extract features from fMRI $\mathcal{H}_{\text{fMRI}}$ and image $\mathcal{H}_{\text{image}}$ latent space, $\mathcal{H} \in \mathbb{R}^{768}$, and features $\mathcal{F} \in \mathbb{R}^{1536}$ and output prompt learnable vectors $V \in \mathbb{R}^8$ for the text encoder. The vectors will be concatenated with tokenized text together input to the CLIP text encoder. Unlike CLIP text and image encoders, the gradients of the Meta-Net were not frozen during the contrastive training, where the Meta-Net was continuously trained and learnable.

Diffusion Model In this study, we introduce a novel approach to fMRI decoding by proposing a diffusion prior integrated within a flexible diffusion model during the training phase. We design the diffusion prior with adjustable parameters, ensuring these are the only elements subject to learning while training the diffusion part. Distinctly, the training of the diffusion model progresses independently from the contrastive learning process. This method leverages latent fMRI features $\mathcal{H}_{\text{fMRI}}$, extracted by an fMRI encoder, which has been refined via contrastive learning across three modalities. To streamline our model, we eliminated the text and image encoders, retaining solely the fMRI encoder that produces latent $\mathcal{H}_{\text{fMRI}} \in \mathbb{R}^{768}$. The foundation of our diffusion prior is based on UNet [46], which utilizes the fMRI latent space as a conditional input. The primary function of this prior is to transform the fMRI latent into image latent space suitable for further processing. During the training, we incorporate a singular linear layer with weights W to adjust the dimensions of the fMRI latent, effectively transforming them as $\mathcal{H}_{\text{fMRI}_T} = W \times \mathcal{H}_{\text{fMRI}}$, with the transformed latent space having dimensions $\mathcal{H}_{\text{fMRI}_T} \in \mathbb{R}^{257 \times 768}$. Our training process employs an ℓ_2 loss $\mathcal{L}_{\mathcal{D}}$ to measure the discrepancy between the ground-truth image latent $\mathcal{H}_{\text{image}}$, encoded by a pre-trained CLIP image encoder, and the image latent $\mathcal{H}_{\text{image}_D}$ denoised by our diffusion prior from the fMRI latent $\mathcal{H}_{\text{fMRI}_T}$. We enhance the robustness of our model by applying intensive data augmentation techniques to the input fMRI data, including sequence permutation, normalization, and sparse coding. Furthermore, as a regularization strategy, we adjust the impact of the loss by applying a loss multiplier α of 0.3 as $\alpha \mathcal{L}_{\mathcal{D}}$, optimizing the model’s performance and generalization capability.

After the prior training, we also integrate the versatile diffusion model as the decoder to decode the converted image latent from fMRI by the diffusion prior to the actual image. We used 20 steps of diffusion to reconstruct the final image. Additionally, we also apply an image selection technique using our encoder to calculate the CLIP similarity matrix between the reconstructed image and the input fMRI. See details in Appendix. We used our trained fMRI encoder to encode the input fMRI and a pre-trained CLIP image encoder to encode the reconstructed image. We select the best one. In this study, we constructed 2 images at the same time.

Metrics Following previous works [10, 16] measurement for reconstructed images, we used the 50-way-top-1 accuracy classification task to evaluate the semantic correctness of the reconstructed images. As the same process as Chen et al., we used a pre-trained [13, 38] ImageNet1K classifier. Both ground-truth and reconstructed images were input to the classifier, and we checked if the top-1 classification of the generated image matched the ground-truth image classification. This metric straightforwardly examines the reconstructed image’s semantic meaning through classification accuracy. This metric is the most critical since the model is aiming to recover the semantic meaning of the images in this work.

In addition to evaluating reconstructed image semantic meaning, we followed previous works by adopting both low-level and high-level metrics as supplementary evaluation for reconstructed image detail features. In low-level metrics, we used pixel-level correlation(PixCorr) to evaluate the reconstructed

images and ground-truth images. We used two-way identification to compare the second and fifth layers of AlexNet, and the last pooling layer of InceptionV3, and the output layer of the CLIP-Vision model. EffNet-B (Eff) and SwAV-ResNet50 (SwAV) are used to calculate the distance correlation. Please see Ozcelik and VanRullen for more details.

4.3 Whole-Brain Visual Experience Analysis

We propose a self-supervised method for analyzing the semantic mapping of whole-brain responses to distinct groups of stimuli and identifying regions of interest. This method specifically examines the correlation between brain region activities and visual images. For a detailed cluster analysis, the self-supervised approach categorizes these images into five distinct clusters. This clustering enhances our understanding of the nuanced relationships between visual stimuli and brain responses.

Clustering K-Means algorithm is a widely known algorithm for self-supervised clustering. However, K-Means is unreliable when it comes to high dimensional data, i.e., it performs poorly when used directly on images. Hence, we used CLIP Image encoder to encode the image to the image latent space and implemented K-Means on the image latent data as shown in Fig. 3. We clustered the dataset visual stimulus images to 5 clusters. We visualized the image labels in each cluster in a word cloud, where larger word sizes indicated higher word frequency in the image label. We asked ChatGPT-4 of the 5 clusters’ word clouds, and let ChatGPT summarize the word cloud cluster name. ChatGPT summarized the cluster name to: “Pets”, “Outdoor Activities”, “Wild Animals”, “Interiors”, and “Indoor Objects.”

Gradient-based Saliency Map To assess the model’s focus on specific neural networks, we utilized Grad-CAM [50], a gradient-based technique. This method involves tracking the gradients from the target output back through the network layers to the originating fMRI input data. This process helps in pinpointing which areas of the input are most influential in the model’s predictions, where the gradient values are high. In our cluster analysis, the target outputs are the clusters. We created gradient-based saliency map for each cluster. As shown in Fig. 3, we averaged the gradient values from four subjects in the dataset, and we took the top 20 regions for visualization.

Decoding Visual Experiences Beyond the Visual Cortex During the training and reconstruction phases, we incorporated a visual region mask into the fMRI input data. This mask, aligned with the DiFuMO atlas [11], sets the values within the visual regions to zero by following the network mapping scheme to the Yeo 7 networks [63]. Specifically, we applied the mask to all input fMRI data associated with the visual network as defined in the Yeo 7 classification. This masking procedure was consistently maintained throughout the training and image reconstruction processes. The images reconstructed from the fMRI data with the visual networks masked are displayed in Fig. 2. The ablation network ablation of other six networks are the same process described as visual network above.

4.4 Zero-Shot Human Imagination Decoding

We applied our pre-trained WAVE model in a universal setting to the BOLD5000 dataset, aiming for zero-shot reconstruction of images from fMRI imagination recordings. The quality of reconstructed images was evaluated using two-way identification metrics, comparing them to the ground-truth text stimuli. The decoding capability of the model is closely linked to the scale and distribution of the training dataset. To further explore the potential of imagination image decoding, we conducted a scale analysis, contrasting imagination scenarios with training images.

Two-Way-Identification Accuracy To assess the quality of the reconstructed images against the ground truth texts, we utilized the Two-Way-Identification Accuracy metric. This involved using a pre-trained CLIP model to encode n reconstructed images and n ground-truth texts into image embeddings \mathcal{H}_{image} and text embeddings \mathcal{H}_{text} , respectively. We computed the Pearson product-moment correlation coefficients [21], resulting in an image-text coefficient matrix $M \in \mathbb{R}^{n \times n}$. The accuracy for each image was determined by the ratio of row elements with values less than their diagonal counterparts, divided by $n - 1$. The overall two-way identification accuracy is the average of these individual accuracies.

We recruited 24 young subjects, each presented with 20 scenarios accompanied by text descriptions. Utilizing the aforementioned metric, we aggregated the data into a comprehensive coefficient matrix

$M_{all} \in \mathbb{R}^{480 \times 480}$, and performed a permutation test 5,000 times by randomizing the sequence of image embeddings.

Scale Analysis In our scale analysis, we constructed a scenario-based image-text coefficient matrix $M_{sc} \in \mathbb{R}^{24 \times 24}$ to quantify the scenario-based accuracies. To further explore the interplay between each scenario and the images from the WAVE training set, we computed the cosine distances, resulting in a cosine distance matrix $M_d \in \mathbb{R}^{24 \times 4803}$. This matrix represents the distances between the textual descriptions of each scenario and the 4,803 training images. To synthesize these relationships into actionable insights, the mean cosine distance was calculated for each scenario using the formula:

$$D_{mc} = \frac{1}{|U| \times |V|} \sum_{u \in U} \sum_{v \in V} \left(1 - \frac{u \cdot v}{\|u\|_2 \|v\|_2} \right). \quad (3)$$

In Eq. 3, U and V are the sets of vector representations for the scenario texts and image features respectively, both with dimensionality 768, where $|U| = 24$ and $|V| = 4803$. The formula calculates the average cosine distance across all pairs formed between a vector u in U and a vector v in V , with $u \cdot v$ denoting the dot product and $\|u\|_2$, $\|v\|_2$ their respective Euclidean norms. The results from this computation are depicted in Fig. 4, illustrating the nuanced relationship between textual scenarios and visual training data.

5 Acknowledgement

This research is supported by the HAI-Google Research Award, UST, HAI Hoffman-Yee Grant, and National Institutes of Health grants NIH U24AG072701 and R01AG089169. We also greatly thank Yurong Liu from New York University, for providing figure suggestions and proofreading.

6 Code availability

To ensure the reproducibility of our analyses, we have made our code and processed data publicly available. These resources can be accessed via our GitHub repository at <https://github.com/PPWangyc/WAVE>. See more details at our project website: <https://wave-brain.github.io>.

7 Data availability

Our processed datasets and pre-trained models are available in our Hugging Face collection. Specifically, the processed Whole-Brain BOLD5000 dataset is available at <https://huggingface.co/datasets/PPWangyc/WAVE-BOLD5000>, where you can also find our pre-trained models at <https://huggingface.co/PPWangyc/WAVE-models>. Additionally, accessing the extra validation dataset of fMRI imagination requires IRB approval and a Data Use Agreement (DUA). For more information or to request access, please contact us directly.

References

- [1] Laurence Aitchison and Máté Lengyel. With or without you: predictive coding and bayesian inference in the brain. *Current opinion in neurobiology*, 46:219–227, 2017.
- [2] Andrew James Anderson and Feng Lin. How pattern information analyses of semantic brain activity elicited in language comprehension could contribute to the early identification of alzheimer’s disease. *NeuroImage: Clinical*, 22:101788, 2019.
- [3] Andrew James Anderson, Kelsey McDermott, Brian Rooks, Kathi L Heffner, David Dodell-Feder, and Feng V Lin. Decoding individual identity from brain activity elicited in imagining common experiences. *Nature communications*, 11(1):5916, 2020.
- [4] Roman Belyi, Guy Gaziv, Assaf Hoogi, Francesca Strappini, Tal Golan, and Michal Irani. From voxels to pixels and back: Self-supervision in natural-image reconstruction from fmri. *Advances in Neural Information Processing Systems*, 32, 2019.
- [5] Rishi Bommasani, Drew A Hudson, Ehsan Adeli, Russ Altman, Simran Arora, Sydney von Arx, Michael S Bernstein, Jeannette Bohg, Antoine Bosselut, Emma Brunskill, et al. On the opportunities and risks of foundation models. *arXiv preprint arXiv:2108.07258*, 2021.
- [6] Talia Brandman, Rafael Malach, and Erez Simony. The surprising role of the default mode network in naturalistic perception. *Communications biology*, 4(1):79, 2021.
- [7] Gyorgy Buzsaki. *The brain from inside out*. Oxford University Press, USA, 2019.
- [8] Mathilde Caron, Ishan Misra, Julien Mairal, Priya Goyal, Piotr Bojanowski, and Armand Joulin. Unsupervised learning of visual features by contrasting cluster assignments. *Advances in neural information processing systems*, 33:9912–9924, 2020.
- [9] Nadine Chang, John A Pyles, Austin Marcus, Abhinav Gupta, Michael J Tarr, and Elissa M Aminoff. Bold5000, a public fmri dataset while viewing 5000 visual images. *Scientific data*, 6(1):49, 2019.
- [10] Zijiao Chen, Jiaxin Qing, Tiange Xiang, Wan Lin Yue, and Juan Helen Zhou. Seeing beyond the brain: Conditional diffusion model with sparse masked modeling for vision decoding. In *Proceedings of the IEEE/CVF Conference on Computer Vision and Pattern Recognition*, pages 22710–22720, 2023.
- [11] Kamalaker Dadi, Gaël Varoquaux, Antonia Machlouzariides-Shalit, Krzysztof J Gorgolewski, Demian Wassermann, Bertrand Thirion, and Arthur Mensch. Fine-grain atlases of functional modes for fmri analysis. *NeuroImage*, 221:117126, 2020.
- [12] Jia Deng, Wei Dong, Richard Socher, Li-Jia Li, Kai Li, and Li Fei-Fei. Imagenet: A large-scale hierarchical image database. In *2009 IEEE conference on computer vision and pattern recognition*, pages 248–255. Ieee, 2009.
- [13] Alexey Dosovitskiy, Lucas Beyer, Alexander Kolesnikov, Dirk Weissenborn, Xiaohua Zhai, Thomas Unterthiner, Mostafa Dehghani, Matthias Minderer, Georg Heigold, Sylvain Gelly, et al. An image is worth 16x16 words: Transformers for image recognition at scale. *arXiv preprint arXiv:2010.11929*, 2020.
- [14] Oscar Esteban, Christopher J Markiewicz, Ross W Blair, Craig A Moodie, A Ilkay Isik, Asier Erramuzpe, James D Kent, Mathias Goncalves, Elizabeth DuPre, Madeleine Snyder, et al. fmriprep: a robust preprocessing pipeline for functional mri. *Nature methods*, 16(1):111–116, 2019.
- [15] Karl J Friston, Jean Daunizeau, and Stefan J Kiebel. Reinforcement learning or active inference? *PloS one*, 4(7):e6421, 2009.
- [16] Guy Gaziv, Roman Belyi, Niv Granot, Assaf Hoogi, Francesca Strappini, Tal Golan, and Michal Irani. Self-supervised natural image reconstruction and large-scale semantic classification from brain activity. *NeuroImage*, 254:119121, 2022.
- [17] Ian Goodfellow, Yoshua Bengio, and Aaron Courville. *Deep learning*. MIT press, 2016.

- [18] Caterina Gratton, Steven M Nelson, and Evan M Gordon. Brain-behavior correlations: Two paths toward reliability. *Neuron*, 110(9):1446–1449, 2022.
- [19] Marie-Hélène Grosbras, Susan Beaton, and Simon B Eickhoff. Brain regions involved in human movement perception: A quantitative voxel-based meta-analysis. *Human brain mapping*, 33(2): 431–454, 2012.
- [20] J Swaroop Guntupalli, Michael Hanke, Yaroslav O Halchenko, Andrew C Connolly, Peter J Ramadge, and James V Haxby. A model of representational spaces in human cortex. *Cerebral cortex*, 26(6):2919–2934, 2016.
- [21] Charles R Harris, K Jarrod Millman, Stéfan J Van Der Walt, Ralf Gommers, Pauli Virtanen, David Cournapeau, Eric Wieser, Julian Taylor, Sebastian Berg, Nathaniel J Smith, et al. Array programming with numpy. *Nature*, 585(7825):357–362, 2020.
- [22] Tong He, Lijun An, Pansheng Chen, Jianzhong Chen, Jiashi Feng, Danilo Bzdok, Avram J Holmes, Simon B Eickhoff, and BT Thomas Yeo. Meta-matching as a simple framework to translate phenotypic predictive models from big to small data. *Nature neuroscience*, 25(6):795–804, 2022.
- [23] David H Hubel and Torsten N Wiesel. Effects of monocular deprivation in kittens. *Naunyn-Schmiedeberg's Archiv für Experimentelle Pathologie und Pharmakologie*, 248:492–497, 1964.
- [24] Trevor Huff, Navid Mahabadi, and Prasanna Tadi. Neuroanatomy, visual cortex. 2018.
- [25] Alexander G Huth, Wendy A De Heer, Thomas L Griffiths, Frédéric E Theunissen, and Jack L Gallant. Natural speech reveals the semantic maps that tile human cerebral cortex. *Nature*, 532(7600):453–458, 2016.
- [26] Yukiyasu Kamitani and Frank Tong. Decoding the visual and subjective contents of the human brain. *Nature neuroscience*, 8(5):679–685, 2005.
- [27] Muhammad Uzair Khattak, Hanoona Rasheed, Muhammad Maaz, Salman Khan, and Fahad Shahbaz Khan. Maple: Multi-modal prompt learning. In *Proceedings of the IEEE/CVF Conference on Computer Vision and Pattern Recognition*, pages 19113–19122, 2023.
- [28] Nikolaus Kriegeskorte and Jörn Diedrichsen. Peeling the onion of brain representations. *Annual review of neuroscience*, 42:407–432, 2019.
- [29] Nikolaus Kriegeskorte, Marieke Mur, and Peter A Bandettini. Representational similarity analysis—connecting the branches of systems neuroscience. *Frontiers in systems neuroscience*, 2:249, 2008.
- [30] Alex Krizhevsky, Ilya Sutskever, and Geoffrey E Hinton. Imagenet classification with deep convolutional neural networks. *Advances in neural information processing systems*, 25, 2012.
- [31] Yann LeCun, Yoshua Bengio, and Geoffrey Hinton. Deep learning. *nature*, 521(7553):436–444, 2015.
- [32] Tsung-Yi Lin, Michael Maire, Serge Belongie, James Hays, Pietro Perona, Deva Ramanan, Piotr Dollár, and C Lawrence Zitnick. Microsoft coco: Common objects in context. In *Computer Vision—ECCV 2014: 13th European Conference, Zurich, Switzerland, September 6–12, 2014, Proceedings, Part V 13*, pages 740–755. Springer, 2014.
- [33] Scott Marek and Nico UF Dosenbach. The frontoparietal network: function, electrophysiology, and importance of individual precision mapping. *Dialogues in clinical neuroscience*, 20(2):133–140, 2018.
- [34] Scott Marek, Brenden Tervo-Clemmens, Finnegan J Calabro, David F Montez, Benjamin P Kay, Alexander S Hatoum, Meghan Rose Donohue, William Foran, Ryland L Miller, Timothy J Hendrickson, et al. Reproducible brain-wide association studies require thousands of individuals. *Nature*, 603(7902):654–660, 2022.
- [35] Christopher J Markiewicz, Krzysztof J Gorgolewski, Franklin Feingold, Ross Blair, Yaroslav O Halchenko, Eric Miller, Nell Hardcastle, Joe Wexler, Oscar Esteban, Mathias Goncavles, et al. The openneuro resource for sharing of neuroscience data. *Elife*, 10:e71774, 2021.
- [36] Kenneth A Norman, Sean M Polyn, Greg J Detre, and James V Haxby. Beyond mind-reading: multi-voxel pattern analysis of fmri data. *Trends in cognitive sciences*, 10(9):424–430, 2006.

- [37] Furkan Ozcelik and Rufin VanRullen. Natural scene reconstruction from fmri signals using generative latent diffusion. *Scientific Reports*, 13(1):15666, 2023.
- [38] Adam Paszke, Sam Gross, Soumith Chintala, Gregory Chanan, Edward Yang, Zachary DeVito, Zeming Lin, Alban Desmaison, Luca Antiga, and Adam Lerer. Automatic differentiation in pytorch. 2017.
- [39] Michael R Pinsky and Didier Payen. Functional hemodynamic monitoring. *Critical Care*, 9:1–7, 2005.
- [40] Russell A Poldrack. Inferring mental states from neuroimaging data: from reverse inference to large-scale decoding. *Neuron*, 72(5):692–697, 2011.
- [41] Jonathan D Power, Mark Plitt, Timothy O Laumann, and Alex Martin. Sources and implications of whole-brain fmri signals in humans. *Neuroimage*, 146:609–625, 2017.
- [42] Alec Radford, Jeffrey Wu, Rewon Child, David Luan, Dario Amodei, Ilya Sutskever, et al. Language models are unsupervised multitask learners. *OpenAI blog*, 1(8):9, 2019.
- [43] Alec Radford, Jong Wook Kim, Chris Hallacy, Aditya Ramesh, Gabriel Goh, Sandhini Agarwal, Girish Sastry, Amanda Askell, Pamela Mishkin, Jack Clark, et al. Learning transferable visual models from natural language supervision. In *International conference on machine learning*, pages 8748–8763. PMLR, 2021.
- [44] Aditya Ramesh, Prafulla Dhariwal, Alex Nichol, Casey Chu, and Mark Chen. Hierarchical text-conditional image generation with clip latents. *arXiv preprint arXiv:2204.06125*, 1(2):3, 2022.
- [45] Robin Rombach, Andreas Blattmann, Dominik Lorenz, Patrick Esser, and Björn Ommer. High-resolution image synthesis with latent diffusion models. In *Proceedings of the IEEE/CVF conference on computer vision and pattern recognition*, pages 10684–10695, 2022.
- [46] Olaf Ronneberger, Philipp Fischer, and Thomas Brox. U-net: Convolutional networks for biomedical image segmentation. In *Medical image computing and computer-assisted intervention–MICCAI 2015: 18th international conference, Munich, Germany, October 5-9, 2015, proceedings, part III 18*, pages 234–241. Springer, 2015.
- [47] Olga Russakovsky, Jia Deng, Hao Su, Jonathan Krause, Sanjeev Satheesh, Sean Ma, Zhiheng Huang, Andrej Karpathy, Aditya Khosla, Michael Bernstein, et al. Imagenet large scale visual recognition challenge. *International journal of computer vision*, 115:211–252, 2015.
- [48] Andrei A Rusu, Neil C Rabinowitz, Guillaume Desjardins, Hubert Soyer, James Kirkpatrick, Koray Kavukcuoglu, Razvan Pascanu, and Raia Hadsell. Progressive neural networks. *arXiv preprint arXiv:1606.04671*, 2016.
- [49] Paul Scotti, Atmadeep Banerjee, Jimmie Goode, Stepan Shabalin, Alex Nguyen, Aidan Dempster, Nathalie Verlinde, Elad Yundler, David Weisberg, Kenneth Norman, et al. Reconstructing the mind’s eye: fmri-to-image with contrastive learning and diffusion priors. *Advances in Neural Information Processing Systems*, 36, 2024.
- [50] Ramprasaath R Selvaraju, Michael Cogswell, Abhishek Das, Ramakrishna Vedantam, Devi Parikh, and Dhruv Batra. Grad-cam: visual explanations from deep networks via gradient-based localization. *International journal of computer vision*, 128:336–359, 2020.
- [51] Adam Steel, Edward H Silson, Brenda D Garcia, and Caroline E Robertson. A retinotopic code structures the interaction between perception and memory systems. *Nature Neuroscience*, pages 1–9, 2024.
- [52] Jingyuan Sun, Mingxiao Li, Zijiao Chen, Yunhao Zhang, Shaonan Wang, and Marie-Francine Moens. Contrast, attend and diffuse to decode high-resolution images from brain activities. *Advances in Neural Information Processing Systems*, 36, 2024.
- [53] Yu Takagi and Shinji Nishimoto. High-resolution image reconstruction with latent diffusion models from human brain activity. In *Proceedings of the IEEE/CVF Conference on Computer Vision and Pattern Recognition*, pages 14453–14463, 2023.

- [54] Mingxing Tan and Quoc Le. Efficientnet: Rethinking model scaling for convolutional neural networks. In *International conference on machine learning*, pages 6105–6114. PMLR, 2019.
- [55] Armin Thomas, Christopher Ré, and Russell Poldrack. Self-supervised learning of brain dynamics from broad neuroimaging data. *Advances in neural information processing systems*, 35:21255–21269, 2022.
- [56] Mark A Thornton and Diana I Tamir. Neural representations of situations and mental states are composed of sums of representations of the actions they afford. *Nature Communications*, 15(1):620, 2024.
- [57] David C Van Essen, Stephen M Smith, Deanna M Barch, Timothy EJ Behrens, Essa Yacoub, Kamil Ugurbil, Wu-Minn HCP Consortium, et al. The wu-minn human connectome project: an overview. *Neuroimage*, 80:62–79, 2013.
- [58] Ashish Vaswani, Noam Shazeer, Niki Parmar, Jakob Uszkoreit, Llion Jones, Aidan N Gomez, Łukasz Kaiser, and Illia Polosukhin. Attention is all you need. *Advances in neural information processing systems*, 30, 2017.
- [59] Pauli Virtanen, Ralf Gommers, Travis E Oliphant, Matt Haberland, Tyler Reddy, David Cournapeau, Evgeni Burovski, Pearu Peterson, Warren Weckesser, Jonathan Bright, et al. Scipy 1.0: fundamental algorithms for scientific computing in python. *Nature methods*, 17(3):261–272, 2020.
- [60] Simone Vossel, Joy J Geng, and Gereon R Fink. Dorsal and ventral attention systems: distinct neural circuits but collaborative roles. *The Neuroscientist*, 20(2):150–159, 2014.
- [61] Xingqian Xu, Zhangyang Wang, Gong Zhang, Kai Wang, and Humphrey Shi. Versatile diffusion: Text, images and variations all in one diffusion model. In *Proceedings of the IEEE/CVF International Conference on Computer Vision*, pages 7754–7765, 2023.
- [62] Lingxiao Yang, Ru-Yuan Zhang, Yanchen Wang, and Xiaohua Xie. Mma: Multi-modal adapter for vision-language models. In *Proceedings of the IEEE/CVF Conference on Computer Vision and Pattern Recognition (CVPR)*, 2024.
- [63] BT Thomas Yeo, Fenna M Krienen, Jorge Sepulcre, Mert R Sabuncu, Danial Lashkari, Marisa Hollinshead, Joshua L Roffman, Jordan W Smoller, Lilla Zöllei, Jonathan R Polimeni, et al. The organization of the human cerebral cortex estimated by intrinsic functional connectivity. *Journal of neurophysiology*, 2011.
- [64] Yaara Yeshurun, Mai Nguyen, and Uri Hasson. The default mode network: where the idiosyncratic self meets the shared social world. *Nature reviews neuroscience*, 22(3):181–192, 2021.
- [65] Kaiyang Zhou, Jingkang Yang, Chen Change Loy, and Ziwei Liu. Conditional prompt learning for vision-language models. In *Proceedings of the IEEE/CVF conference on computer vision and pattern recognition*, pages 16816–16825, 2022.

A Appendix / Supplemental Material

A.1 Individual Decoding Result

Whole Brain Decoding. In our main paper, we present two experiment settings, the individual model for decoding and the universal model. To explore our WAVE model decoding ability for individual subjects. We provide each subject metric results here. As shown in the Table 3. We showed all four subjects in the BOLD5000 dataset, and each subject ID is listed in the first column, and the details metrics results are followed in each row. WAVE has great advances in decoding semantic meaning from the fMRI and the results in High-Level and Semantic Top-1 Accuracy also prove this point.

Table 3: **Individual Subject Reconstructed image evaluation metrics.** We extend our averaged across subject result table in manuscript to individual result. All the metrics are the same setting as the manuscript.

Subject	Model	Low-Level				High-Level				Semantic
		PixCorr \uparrow	SSIM \uparrow	AlexNet(2) \uparrow	AlexNet(5) \uparrow	Incep \uparrow	CLIP \uparrow	Eff \downarrow	SwAV \downarrow	Top-1 Acc \uparrow
CSI1	WAVE (Ours)	0.078	0.230	76.29%	83.00%	75.20%	86.37%	0.859	0.539	33.28%
	MindEye [49]	0.079	0.226	76.90%	84.06%	67.67%	67.67%	0.895	0.566	17.78%
	Mind-Vis [10]	0.095	0.313	73.81%	82.18%	74.02%	70.07%	0.877	0.514	23.64%
CSI2	WAVE (Ours)	0.061	0.167	72.38%	82.74%	72.06%	82.71%	0.890	0.548	28.53%
	MindEye [49]	0.046	0.218	67.14%	72.18%	60.99%	68.09%	0.940	0.616	11.01%
	Mind-Vis [10]	0.076	0.320	69.90%	77.09%	68.39%	70.07%	0.906	0.546	16.04%
CSI3	WAVE (Ours)	0.063	0.208	70.14%	78.67%	65.40%	80.04%	0.898	0.550	23.00%
	MindEye [49]	0.031	0.218	69.95%	73.32%	64.68%	67.53%	0.934	0.611	14.32%
	Mind-Vis [10]	0.085	0.316	68.66%	74.98%	66.20%	70.07%	0.912	0.553	16.40%
CSI4	WAVE (Ours)	0.045	0.193	67.60%	74.38%	62.38%	77.04%	0.922	0.572	16.15%
	MindEye [49]	0.068	0.207	70.49%	79.69%	71.99%	76.64%	0.895	0.574	24.27%
	Mind-Vis [10]	0.043	0.286	57.33%	56.73%	59.08%	58.15%	0.961	0.610	14.55%

Visual Network Mask Decoding. Besides presenting the decoding results from whole brain wise data (WAVE) and visual cortex data (MindEye & Mind-Vis), we also explored decoding information from brain regions that do not belong to the visual networks. By applying the mask to the input fMRI data, WAVE can still successfully decode the natural image from fMRI across all subjects. In addition to the averaged subject results in the manuscript, we also provide the individual visual networks mask results in Table 4. Our individual visual mask result gives new insights into neuroscience to understand various brain regions’ functions not only at visual perception level, but in the cognition. Compared with the whole brain individual decoding results in Fig. 3, the visual masked metrics across subjects are slightly lower.

Table 4: **Individual Subject visual network masked decoding results.** The brain regions belonging to the visual network according to Yeo 7 Atlas were masked in the fMRI input. The base model is WAVE.

Subject	Low-Level				High-Level				Semantic
	PixCorr \uparrow	SSIM \uparrow	AlexNet(2) \uparrow	AlexNet(5) \uparrow	Incep \uparrow	CLIP \uparrow	Eff \downarrow	SwAV \downarrow	Top-1 Acc \uparrow
CSI1	0.059	0.191	67.75%	78.52%	70.12%	82.35%	0.881	0.558	25.95%
CSI2	0.053	0.185	67.31%	75.43%	67.42%	78.58%	0.911	0.591	17.40%
CSI3	0.033	0.176	65.41%	75.43%	62.49%	75.73%	0.920	0.600	18.78%
CSI4	0.041	0.193	66.10%	71.11%	62.62%	75.63%	0.925	0.603	13.79%

Ablation Studies. We conducted ablation studies to evaluate the performance of different encoder and decoder configurations in diffusion-based image reconstruction. Two types of encoders were used: the pre-trained fMRI Foundation model and the train-from-scratch MLP Backbone. For the decoders, we explored two diffusion models: Versatile Diffusion and Stable Diffusion. The ablation results, presented in Table 5, indicate that the fMRI Model, which employs a region encoder [55], demonstrates superior performance compared to the MLP Backbone. Additionally, Versatile Diffusion consistently outperformed Stable Diffusion across evaluated metrics.

In addition to exploring various encoder and decoder configurations, our research extended to analyzing the impact of decoder loss functions on Subject CSI3. Our findings indicate that utilizing diffusion model loss directly on image pixel values, rather than on embeddings, enhances performance in low-level

Table 5: **Encoder and Decoder Ablation Studies on Subject CSI3.** This table details our ablation studies comparing the Versatile and Stable diffusion models. Different encoder configurations were tested: the region encoder utilizes whole brain data, while the voxel encoder targets the visual cortex fMRI specifically. The fMRI Model refers to the pre-trained fMRI Foundation model, and the MLP Backbone is a custom-built residual MLP model. We assessed the models based on semantic accuracy and Fréchet Inception Distance (FID), with lower FID values indicating better image reconstruction quality.

fMRI Encoder		Decoder	Acc(%)	Min(%)	Max(%)	FID	Min	Max
Region Enc	Voxel Enc							
fMRI Model (Thomas et al.)	w/o	VD	22.13 ± 1.48	19.62	23.41	2.45 ± 0.71	1.68	3.55
fMRI Model (Thomas et al.)	w/o	SD	18.81 ± 1.17	17.87	20.46	3.70 ± 1.48	2.37	5.77
MLP Backbone	w/o	VD	18.79 ± 1.72	16.71	20.92	4.81 ± 0.95	3.53	5.80
MLP Backbone	w/o	SD	13.03 ± 0.95	12.17	14.35	6.69 ± 1.55	4.94	8.70
w/o	MLP Backbone	VD	12.91 ± 1.12	11.41	14.09	3.65 ± 0.63	3.09	4.53
w/o	MLP Backbone	SD	10.41 ± 1.00	9.01	11.23	6.62 ± 1.36	4.87	8.20

pixel-related metrics and Fréchet Inception Distance (FID). As demonstrated in Table 6, Mind-Vis [10] has better low-level performance.

Table 6: **Decoding loss ablation on Subject CSI3.** This table compares the performance of different models based on the type of loss function used, whether applied directly to the image pixels or to the latent embedding space. WAVE and MindEye utilize an embedding-based loss, whereas Mind-Vis employs a pixel-based loss with a Latent Diffusion Model (LDM) as the decoder.

Model	Loss	Decoder	Acc(%)	Min(%)	Max(%)	FID	Min	Max
WAVE	Embed	VD	22.13 ± 1.48	19.62	23.41	2.45 ± 0.71	1.68	3.55
MindEye (Scotti et al.)	Embed	VD	13.45 ± 0.13	12.89	14.97	2.91 ± 0.39	2.53	3.30
Mind-Vis (Chen et al.)	Pixel	LDM	14.83 ± 2.25	12.59	19.08	1.64 ± 0.19	1.40	1.98

Additionally, we also conduct research to show multi-modal fMRI-Visual-Language learning with prompt Meta-Net effect in this decoding task. As illustrated in Table 7, incorporating multiple modalities through contrastive learning enhances the model’s ability to encode representations, thereby improving the classification accuracy for Brain (fMRI) and Vision (Visual Stimulus) using the CLIP model. The introduction of prompt-based learning further aids in balancing the training across multiple modalities, enhancing both Brain-Vision and Brain-Language accuracy.

Table 7: **Ablation Study for the Contrastive Learning Method on Subject CSI3.** This table presents the ablation results comparing the Brain-Vision contrastive learning model, which involves only visual stimulus and fMRI data, with models that include Brain-Vision-Language triple modality contrastive learning and Meta-Net Prompt triple modality learning. The evaluation metrics include Top-1 classification accuracy for CLIP, along with Brain to Vision Accuracy and Brain to Language Accuracy.

Model	Brain-Vision Accuracy (%)	Brain-Language Accuracy (%)
Vision Only	43.96%	20.0%
Vision + Language w/o Prompt	49.44%	34.81%
Vision + Language w/ Prompt (WAVE)	53.98%	36.28%

fMRI Embedding. In this study, we compare raw fMRI embeddings with our WAVE-encoded fMRI embeddings using a t-SNE visualization as depicted in Figure 6. Typically, raw fMRI data visualized without encoding appears scrambled and indistinguishable across different clusters. In contrast, the WAVE-encoded fMRI embeddings clearly delineate distinctions between clusters. This distinction suggests that our WAVE model is effectively capturing the salient features of whole-brain fMRI signals.

A.2 Method

Training Details. For our training process, we consistently utilized a seed value of 42. We employed an Adam optimizer, setting the learning rate at 1×10^{-4} . The decay rates were configured differently

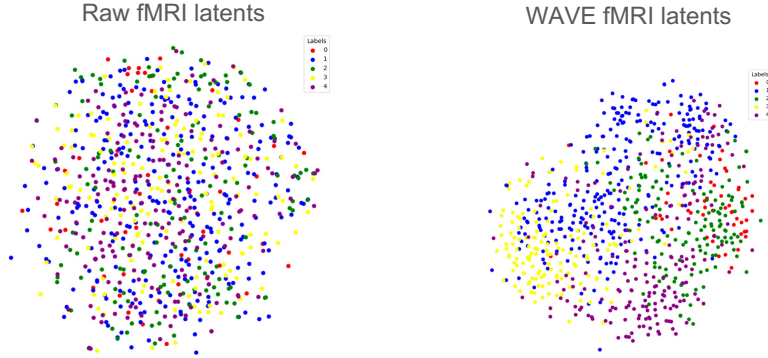


Figure 6: **T-SNE plot** depicting raw fMRI latents and WAVE encoded fMRI latents. The WAVE encoding method shows a clear defined separation into 5 clusters compared to the distribution of the raw latents.

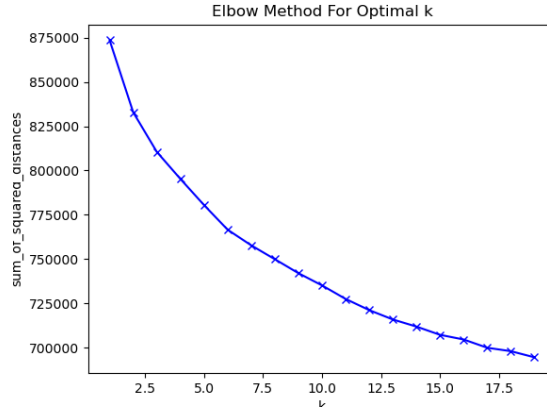


Figure 7: **Elbow Method for identifying the optimal number of clusters:** The reported figure is the sum of squared distance (SSD) versus cluster number K . While the SSD decreases as the number of clusters increases, there is no distinct “elbow” point, which is difficult to determine an optimal cluster number from the curve.

for various components of the training: 0.03 for the contrastive learning part and 0.02 for the diffusion model training. The number of training steps was set to 50,000 for the contrastive learning phase and 200,000 for the diffusion model phase, for each individual model. In the case of universal model training, which involved data from four subjects, we quadrupled the training steps to accommodate the increased data volume.

Compute. All experiments were conducted on single GPU setups. For the contrastive learning phase, we utilized Tesla V100 GPUs with 32GB of memory, where the WAVE models were trained for approximately 6 hours. In contrast, training the decoding diffusion model required significantly more GPU memory and computational power. We used an A-100 GPU with 40GB for this purpose, with the training duration for individual subject decoding approximately 25 hours. For the universal decoding model, which includes data from four subjects, the training time was extended to nearly 80 hours. The model inference also involves a diffusion model and we used one A-100 GPU. For fMRI preprocessing, we only utilized cpu compute nodes.

Clustering. The self-supervised clustering method that we used is k-clustering after the encoded image features by CLIP. It is not easy to determine how many clusters we should use in the analysis. The datasets include broad range of image types and classes, and we also conducted the elbow analysis for better cluster numbers. As we showed in Fig. 7, the sum of the squared distance is decreasing with larger

cluster number. But there is no obvious elbow curve occurs even in 20 clusters. For better clustering analysis purpose, we used 5 clusters for our study.

Metrics. For the evaluation and analysis of our model, we employed various metrics, including the mean cosine distance between scenario text and training images. This metric is computed as described in Equation 3. We provide the Python scipy code [59] used for calculating the mean cosine distance for each scenario texts, as follows:

```
# Calculate cosine distance
from scipy.spatial.distance import cdist
cosine_distances = cdist(image_embeddings, _gt_text_embeddings, metric='cosine')
mean_cosine_distance = np.mean(cosine_distances)
```